Drag Force Regime in Dry and Immersed Granular Media

Jiayu Lin[1], Tao Zhao[3,5*], Mingjing Jiang[2,4*]

[1] School of Civil Engineering, Tianjin University, 300072, China

[2] School of Civil Engineering, Suzhou University of Science and Technology, Suzhou, 215009, China

[3] Department of Civil and Environmental Engineering, Brunel University London, London, UB8 3PH, United Kingdom

[4] College of Civil Engineering, Tongji University, Shanghai 200092, China

[5] Sichuan University, State Key Laboratory of Hydraulics and Mountain River Engineering, 610065, China

***Corresponding authors:**

Dr Tao Zhao; Email: tao.zhao@brunel.ac.uk; Tel: +44 (0)1895 265532; ORCID: 0000-0003-2828-6314

Prof. Mingjing Jiang; Email: mingjing.jiang@tongji.edu.cn

Abstract

The drag force acting on an intruder colliding into the granular media is typically influenced by the impact velocity and penetrating depth. In this study, the investigation was extended to the dry and immersed scenarios through coupled simulations at different constant intrusion velocities. The drag force regime was clarified to exhibit velocity dependence in the initial contact stage, followed by the inertial transit stage with a $F \sim z^2$ (force-depth) relationship. Subsequently, it transitioned into the depth-dependent regime in both dry and immersed cases. The underlying rheological mechanism was explored, revealing that in both dry and immersed scenarios, the granular bulk underwent a state relaxation process, as indicated by the inertial number. Additionally, the presence of the ambient fluid restricted the flow characteristics of the perturbed granular material, exhibiting a similar rheology framework as observed in the dry case.

Introduction

Granular materials exhibit a range of phenomena that resemble macroscopic behavior observed in solids, fluids, and gases, highlighting their unique and universal condensed properties. Despite their significance in engineering and fundamental scientific research [1], a comprehensive and quantitative theory with a solid physical foundation that encompasses all the rich features of granular materials is still lacking. A specific area of investigation focuses on intruder penetration into bulk granular media, a widespread phenomenon encountered in various fields, such as structure-soil interaction in engineering [2], robotics locomotion [3,4], and the astrophysical realm[5]. In addition, intruder penetration in immersed granular media is also ubiquitous in multiple realms, such as soil bed erosion by saturated debris flows [6], penetration tests in marine beds [7] and underwater crater formation in geological fields [8]. This process offers valuable insights into granular behavior, as it occurs in different stages where the substrate media exhibits characteristics of both solids and fluids. This suggests that granular media undergoes phase transitions, determined by its mechanical behavior, as it transitions between different flow regimes [9].

Considerable research efforts have been dedicated to understanding the mechanism of penetration in granular materials. In the quasi-static regime, the resistance encountered during penetration is similar to that of a regular fluid [10,11], and the modified Archimedean law has been used for predictions [12,13]. However, beyond the quasi-static regime, the proportionality of the force F_z to the depth z alone is insufficient. An additional term F_v proportional to the square of the velocity v, representing the inertial effect, is introduced [14-19]. In these cases, the resulting resistance can be estimated by $F(z,v) = F_z(z) + F_v(v^2)$ when the $v > v_c = \sqrt{2gd_g}$, with v_c being the speed of a particle falling under gravity [17]. While the separate contributions of depth and velocity to the drag force are widely discussed in the context of impact processes [14,20,21], the underlying physical justification remains unclear due to the interplay between depth and velocity during the dynamic events. This complexity is further amplified in the immersed case, where the response of the fluid-solid mixture substrate becomes intricate. Consequently, previous investigations on this problem are via either a continuum or discrete approach [9,16,22-28]. However, the isolated mechanisms governing the $F_z(z)$ and $F_v(v^2)$ terms are yet to be fully elucidated. Recent studies [29,30] have shed light on the distinct nature of the $F_v(v^2)$ term, which deviates from theoretical expectations. Nevertheless, a comprehensive understanding of the settlement behavior of granular materials, including momentum transfer and local or nonlocal rheology evidence, remains incomplete, particularly in the context of the immersed case. Here, we try to reveal the underlying mechanism of drag force both in the dry and immersed cases, meanwhile uncovering the analogy and correlation between the two scenarios.

Model description and numerical setup

To investigate the coupling mechanisms between velocity (v) and depth (z) and to examine the influence of the ambient fluid, this study aimed to establish a general numerical approach for understanding the intrusion phenomena. A coupled computational fluid dynamics and discrete element method (CFD-DEM) implemented in the software PFC 3D (Particle Flow Code) and OpenFOAM model was employed to simulate the impact penetration process at a constant velocity (v_0). Unlike previous approaches using homogenized the particles and fluid, the current model explicitly solved the individual motion of particles and fluid [28]. In this study, polydispersed grains were utilized to mimic natural granular packing state and prevent crystallization. The rolling resistance contact model, accounting for angular particle shapes, was incorporated to capture the shape effect [31]. In the immersed case, the fluid and particle motion were derived from the numerical solution of the Navier-Stokes equations and the second Newtonian law, respectively, using a coarse-grid coupled scheme [32].

The simulation setup is depicted in Figure 1(a-b). A frictional spherical intruder with a diameter (D) of 2.2 cm ($6.1d_g$, d_g = mean grain diameter) and a density of 7.8 g/cm³ was initially placed at the bed surface and then forced to penetrate into a granular bed at a constant speed (v_0) ranging from 25 cm/s to 500 cm/s. The bed container dimensions were sufficiently large ($W/D > 10$) to minimize boundary effects, following the size recommendations adopted in the experimental and numerical investigations [29,33]. This configuration also enables the simultaneous capture of both the quasi-static and inertial regimes. The granular bed consisted of grains with a diameter (d_g) in the range of 3.6 ± 1.8 mm, as shown in Figure 1(a), with a density (ρ_g) of 2.6 g/cm³. The particle interactions were governed by a contact model developed based on physical principles where the contact behavior among the normal, shear, rolling, and twisting directions has been related by the integration algorithms in the finite contact area, incorporating parameters such as the effective contact modulus ($E = 7 \times 10^7$ Pa), shape parameter ($\beta = 0.25$), local crushing coefficient ($\xi_c = 4.0$), and friction coefficient ($\mu = 0.5$), the further detail could be found in the Supplemental Material [34]. The granular sample was prepared using the under-compaction multi-layer method (UCM) [35] and consolidated under the influence of gravity ($g = 9.8$ m/s^2). The resulting granular volume packing fraction (ϕ) was 0.61, indicating a dilatation required for flow and the emergence of the breakage of jamming states during the penetration [18,36]. The time step is auto-calibrated by the software during the simulation as $1e^{-6}$ s according to the contact stiffness and particle mass, meanwhile kinematic constraints are applied. In the immersed case, the mesh size is selected as the same as the intruder. Water properties were set for the fluid, with a density (ρ_f) of 1000 kg/m^3 and a kinetic viscosity (ν) of 10^{-6} m^2/s. The time step of fluid is set as 1e^{-4} s fitting the CFL condition, which leads to the exchange frequency equal to 100. Additional detailed information regarding the numerical method and model setup can be found in the Supplementary Material [34].

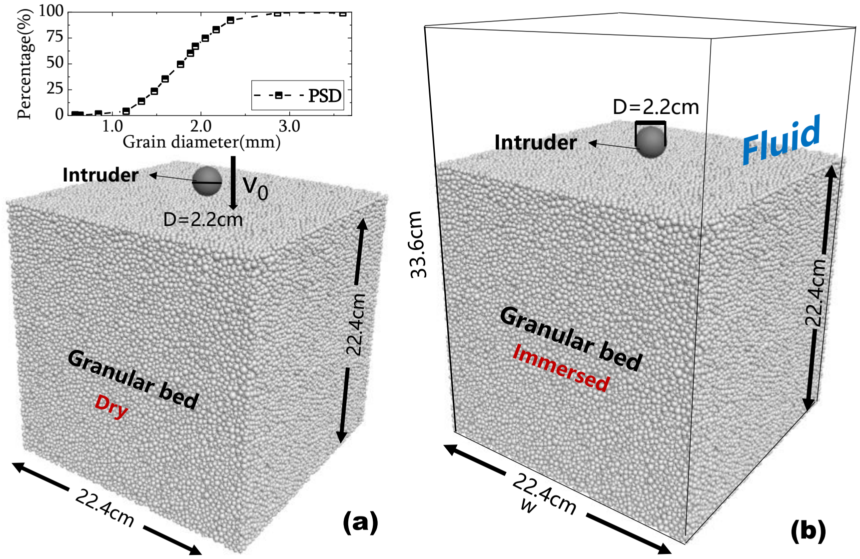

FIG. 1. (a) Particle size distribution (PSD) of polydispersed grains and the numerical model configuration of the dry modelling scenario; (b) numerical model configuration of the immersed modelling scenario.

Results and discussion

A. Drag force evolution

Figure 2(a) displays the evolution of the drag force F(z,v_0) with the dimensionless penetration depth $\tilde{z}$=z/D (normalized by the intruder size) in both the dry and immersed modelling scenarios, recalling the complete phenomenon observed in previous studies [29,37]. Through a comprehensive analysis of the drag force *F*, important insights are gained. Contrary to the expected $F(z,v) = F_z(z) + F_v(v^2)$ relationship depicted in the inset plot of Figure 2(b), both the dry and immersed cases exhibit distinct trends to reach the depth-dependence stage. As indicated in Figure 2(a)-(b), the beginning of the penetration process (referred to as the initial contact stage) exhibits velocity dependence. A sharp peak, denoted as the peak force (F_{peak}), occurs at $\tilde{z}$~0.25, similar to what has been reported in the impact process ($\tilde{z}$~0.125). Subsequently, during the transition stage, fluctuations of varying magnitudes are observed in distinct scenarios (dry and immersed), suggesting the reorganization of the granular medium following intense perturbations [29,30].

Eventually, all F(z,v₀) curves, with different v_0 values, converge into the same increasing slope dF/d$\tilde{z}$ in the dry case (referred to as the depth-dependence stage). In contrast, in the immersed case, though in the depth-dependence stage, the dF/d$\tilde{z}$ is still positively correlated to the penetration velocity. The depth at which the stage transition from 'transition' to 'depth-dependence' occurs is defined as the characteristic depth (z*) and the corresponding F value is referred to as the characteristic force (F*). The ambient fluid affected the penetration process by attenuating the fluctuations and increasing the magnitude level of the drag force F. This effect is evident in the larger characteristic force F* and the subsequent higher dF/d$\tilde{z}$ values in the depth-dependence stage of the immersed case.

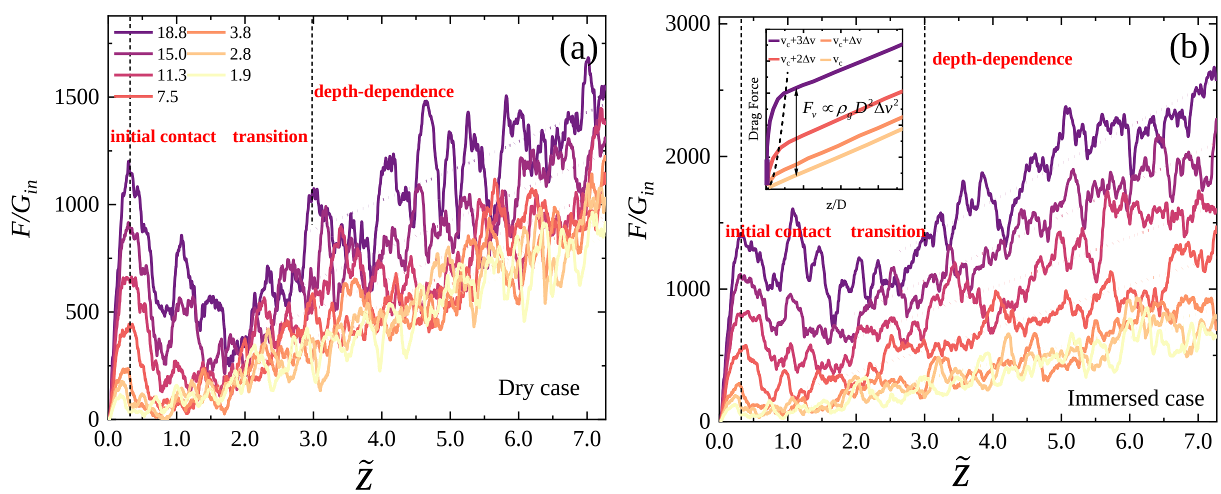

FIG. 2. The drag force offered by granular bulk on a spherical intruder versus z in different speeds in (a) dry and (b) immersed modelling scenarios, respectively. The vertical dashed lines delimit the stages and the inclined dashed lines are the linear fitting. The inset plot in (b): Expected results from the theoretical model, Δv: the incremental penetration velocity of the intruder. The drag force is normalized by the weight of the intruder $G_{in}= m_{in}g$ and the penetration velocity is normalized by the $v_c = \sqrt{2gd_g}$.

B. Regime identification

The distinct intrusion characteristics, including the peak force F_{peak}, characteristic force F^*, and characteristic depth z^*, have been examined in detail to provide a comprehensive description of the different stages. Figure 3(a) presents the scaling law between the peak force F_{peak} and penetration velocity v_0. Interestingly, the linear correlation observed in both the immersed and dry cases contradicts previous findings [29] of a quadratic dependence. However, this linear relationship between F_{peak} and v_0 aligns with experimental results related to drag force in plow or upward drag problems [36,38]. This deviation from the previously observed quadratic dependence can be attributed to the break-up of the jamming state, during which the granular bulk transitions from a static state to a flow regime [39,40]. The dilatancy characteristic of granular material, which was accounted for in this study through rolling and twisting resistances, may contribute to the more intense shear-dilatancy behavior in the dense state. The inset plot in Figure 3(a) demonstrates the gradual convergence of F/v_0 versus $\tilde{z}$ evolution trend, indicating the velocity-dependence characteristic with distinct 'viscous' behavior in this stage. As shown in Figure 2(b), the quadratic scaling law between F^* and v_0 is observed in both the immersed and dry modelling scenarios and imply the 'inertial effect', albeit with different fitting coefficients. Meanwhile similar convergence trend of F/v_0^2 in different ranges of penetration depth can be observed in the inset plot, which indicates the collisional momentum transfer [30]. The observed difference in F^* caused by the ambient fluid in the transition stage indeed deviates from the initial stage which is with a slight difference in F_{peak} caused by the interstitial fluid. This evidence suggests different action mechanisms of fluid in these two different stages (i.e. initial contact, transition). The relationship between z^* and v_0, depicted in Figure 3(c), illustrates the characteristic of dynamic relaxation for the granular bulk during intrusion. The negligible difference between the two cases indicates that the ambient fluid does not affect the intrusion depth required for particle contact network reorganization [41]. Recall the inset plot of Figure 3(b), the consistency between the depth at which F/v_0^2 deviates from the overlapping collapse trend and the corresponding z^* is obtained. This observation indicates the progression towards depth-dependence stage (quasi-static regime) is accompanied by a gradual reduction in the inertial effect, as evidenced by the quadratic velocity dependency relationship.

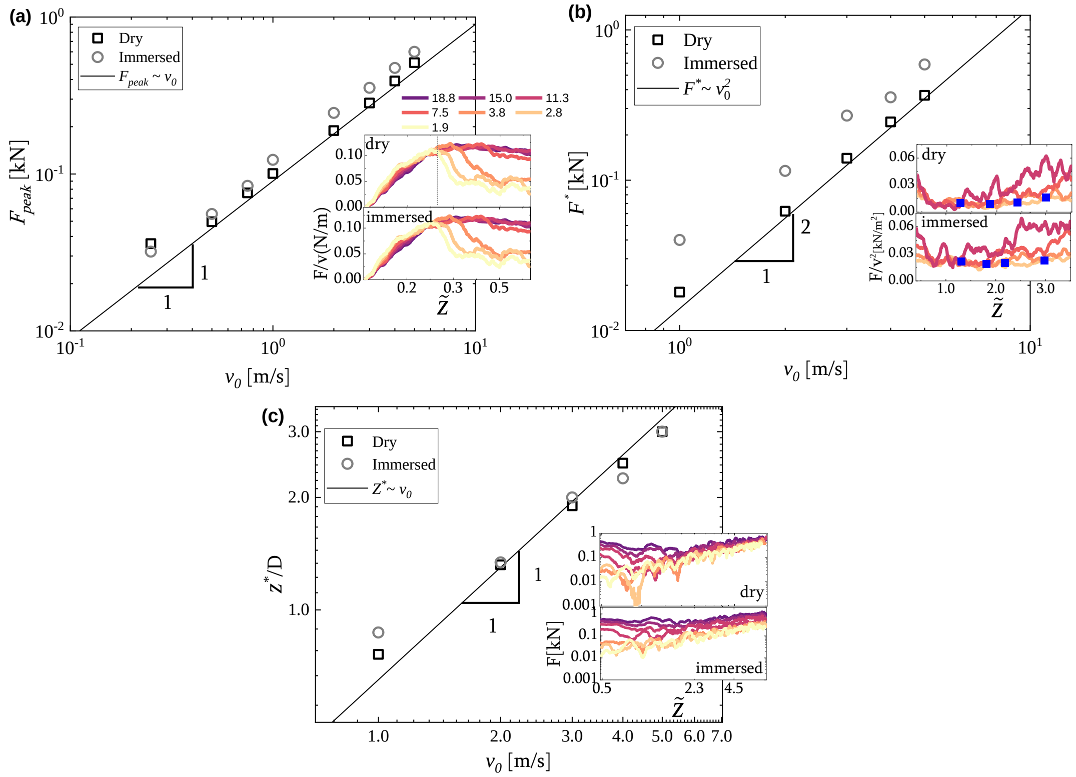

FIG. 3. (a) Correlation between peak force F_{peak} and penetration velocity v_0 . The inset plot is the drag force scaled by the velocity as the function of the penetration depth $\tilde{z}$. (b) Correlation between the characteristic force F^* and penetration velocity v_0. The inset plot is the drag force scaled by the quadratic velocity as the function of the depth $\tilde{z}$, and the separation time is marked as solid blue squares. (c) Correlation between the characteristic depth z^* and the penetration velocity v_0 . The inset plot is the log-log relationship between the drag force F and penetration depth $\tilde{z}$. In (b)(c), the data points corresponding to the intruder velocity less than 1 m/s were ignored due to their weak inertial effect.

Filtering the fluctuations provided by the discrete characteristic of granular media, Fig. 4 presents a schematic extracted trend of the penetration process to reflect the main feature of the drag force evolution, which captures the essential characteristics of the initial contact, transition, and depth-dependence stage. The state curves for the linear $F\sim\tilde{z}$ and quadratic $F\sim\tilde{z}^2$ functions define the boundaries of different stages. Furthermore, the underlying quasi-static and inertial regimes of these stages are also highlighted. In the inset plot of Fig. 4(a), the experimental and numerical data from previous studies [30,42] are summarized, demonstrating the same power law with different coefficients that confirm the generality of the observed behavior. Despite quantitative deviations, the immersed case follows a similar regime hierarchy to the dry case. A comparison with the ideal pattern of the drag force's evolution shown in the inset of Fig. 2(b) suggests a shared underlying physical nature, while highlighting the different approaches to the depth-dependence regime. The theoretical model neglects the state transformation from the jamming state [39,43] in the initial contact stage and the progressive evolution of compound components ($F_z(z)$, $F_v(v)$, and $F_v(v^2)$) in the transition stage, presents a more idealized inheritance mechanism of the inertial effect.

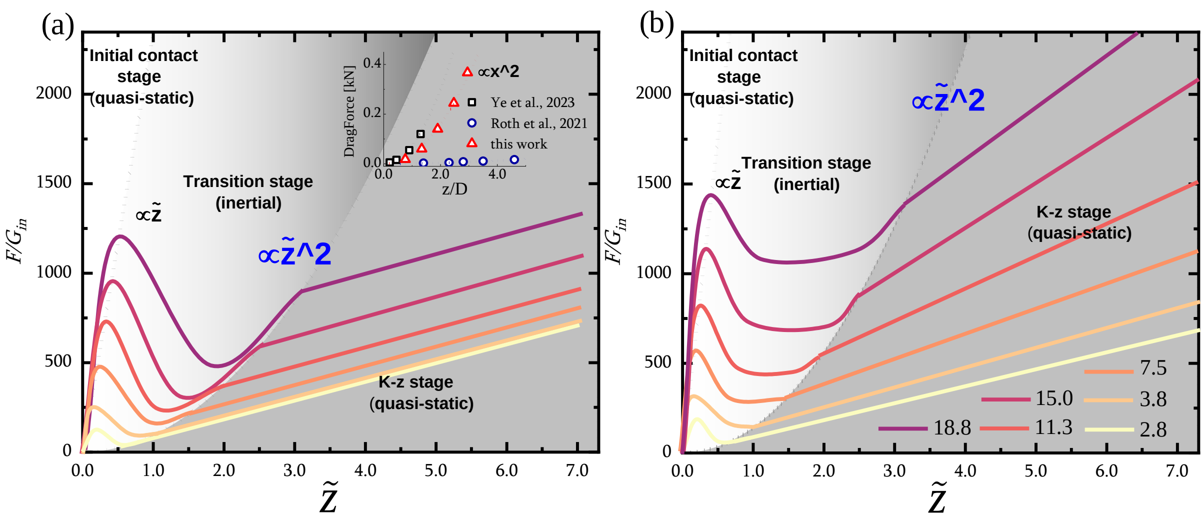

Fig 4 (a) The relationship between $F \sim \tilde{z}$ derived from the numerical results. The delimitation line is marked as the dashed line. The inset plot summarizes the published numerical and experimental results [30,42]. (b) the extracted model adapted to the immersed case. The drag force is normalized by the weight of the intruder $G_{in} = m_{in}g$ and the penetration velocity is normalized by the $v_c = \sqrt{2gd_g}$.

C. Local measurements

For the mechanical analysis, the local rheology measurement [44] is employed to provide a comprehensive understanding of the effect of the ambient fluid and the underlying mechanisms governing dry and immersed granular materials. The variable protocol begins with the decomposition of the strain rate and stress tensor, denoted as $\dot{e}$ and $\boldsymbol{\sigma}$, into isotropic and deviatoric parts: $\dot{e} = \dot{\varepsilon}\boldsymbol{I} + \dot{e}_{\boldsymbol{d}}$ and $\boldsymbol{\sigma} = -p\boldsymbol{I} + \sigma_d$. Here, $\boldsymbol{I}$ represents the unit tensor; $\dot{\varepsilon} = \frac{1}{3}\mathrm{tr}(\dot{e}) = \frac{1}{3}\mathrm{div}\,\mathbf{v}$ is the dilation rate; $\dot{e}_{\boldsymbol{d}}$ is the shear rate tensor; p is the pressure; and σ_d is the shear stress tensor. Scalar quantities corresponding to the invariants of the strain rate and stress tensors are presented, including the dilation rate, pressure, shear rate ($\dot{\gamma}$), and shear stress ($\boldsymbol{\tau}$). Further detailed calculation approaches of the physical field could be found in the Supplementary Material [34]. The analysis focuses on an intermediate penetration velocity (v_0) of 3.0 m/s, chosen to reveal detailed mechanisms. Two measurement circles of the same size as and moving together with the intruder (characteristic length) are selected: the central area directly beneath the intruder and the direct edge next to the intruder at the same vertical position. The spatially averaged approach has been adopted to the lateral monitoring point. As a result, these monitored areas provide insights into the local flow characteristics surrounding the intruder.

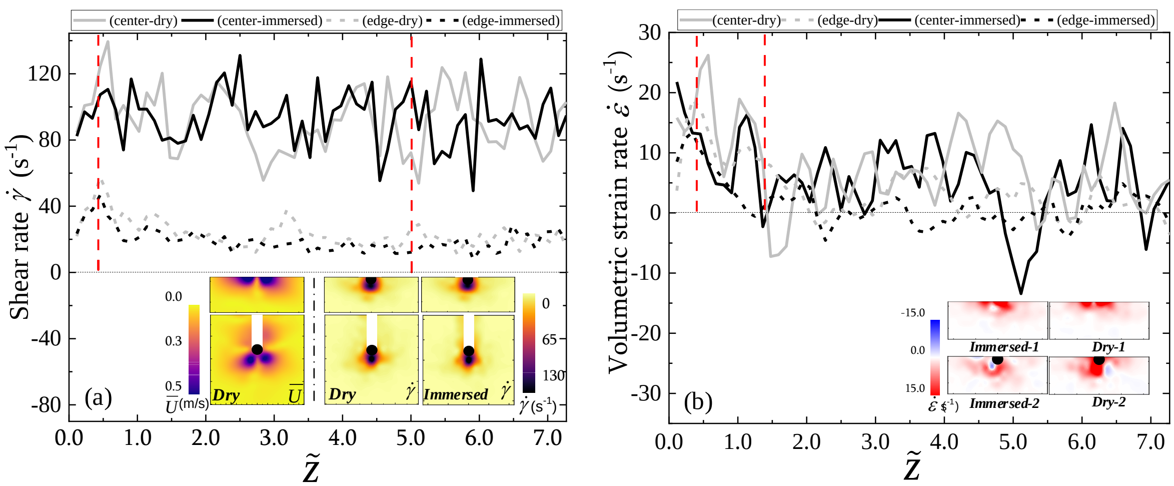

Fig 5 (a)-(b) the evolution of the shear rate $\dot{\gamma}$ and dilation rate $\dot{\varepsilon}$ versus penetration depth $\tilde{z}$ in different regions. The boundary between the dilation and contraction is marked as the horizontal black dashed line in (b). The inset plot is the field distribution of the corresponding properties extracted from the position marked by the vertical red dashed line.

The evolutions of the shear rate ($\dot{\gamma}$) and dilation rate ($\dot{\varepsilon}$) are presented in Fig 5(a) and (b), respectively, while the time-averaged quantities are summarized in Table 1. Throughout the penetration process, $\dot{\gamma}$ remains almost constant, with larger values observed in the central area. On the other hand, $\dot{\varepsilon}$ reaches a stable state once the intruder is fully submerged, with higher values observed in the central area, consistent with $\dot{\gamma}$. The spatial distribution of the relevant physical value is illustrated in the inset plots. From the plot of averaged velocity $\overline{U}$, the symmetric pattern with the stagnant area underneath the intruder was observed, similar to the findings presented in the experiment [45]. The shear-rate contour shows the coincident results as the curves of the main plot that the highest shear rate emerges underneath the intruder. The similar shear-rate evolution pattern between the different depths discussed here is reflected by the stable state mentioned before. As for the volumetric strain rate in the inset plot, the large fluctuations characteristic and the spatial distribution feature could be verified qualitatively. Based on the time-averaged results in Table 1, the effect of the ambient fluid on the strain rate ($\dot{e}$) is identified. The interstitial fluid enhances the shear-dilation behavior in both the edge and central areas, while it has no effect on $\dot{\gamma}$. It can be speculated that this effect of the ambient fluid on the strain rate has a synergistic mechanism with the increased pressure observed in the immersed bulk granular media. This suggests a potential rheological explanation for the influence of the fluid based on the higher pressure in the immersed case.

Table 1 Time-average results of strain-rate

$\langle\dot{\gamma}\rangle(s^{-1})$			$\langle\dot{\varepsilon}\rangle(s^{-1})$		
	Edge	Center		Edge	Center
Immersed	19.075	93.064	Immersed	1.358	5.621
Dry	21.121	92.380	Dry	3.860	7.531

The evolution of stress (including pressure and shear stress) in the central and edge areas is shown in Fig 6(a) and (b), respectively. The significant differences between these two locations indicate the localization of stress beneath the intruder and the emergence of higher stress in the immersed case, providing a mesoscale explanation for the influence of the ambient fluid on the macroscopic drag force. Furthermore, the consistent evolution patterns between shear stress ($\boldsymbol{\tau}$), pressure (p), and drag force (F in Fig. 2) suggest that the resistance is determined by the integration of stress applied to the interface. From the contour, the concentrated stress appears in the bottom area of the intruder meanwhile the larger stress level in the immersed case could also be distinguished from the pattern feature.

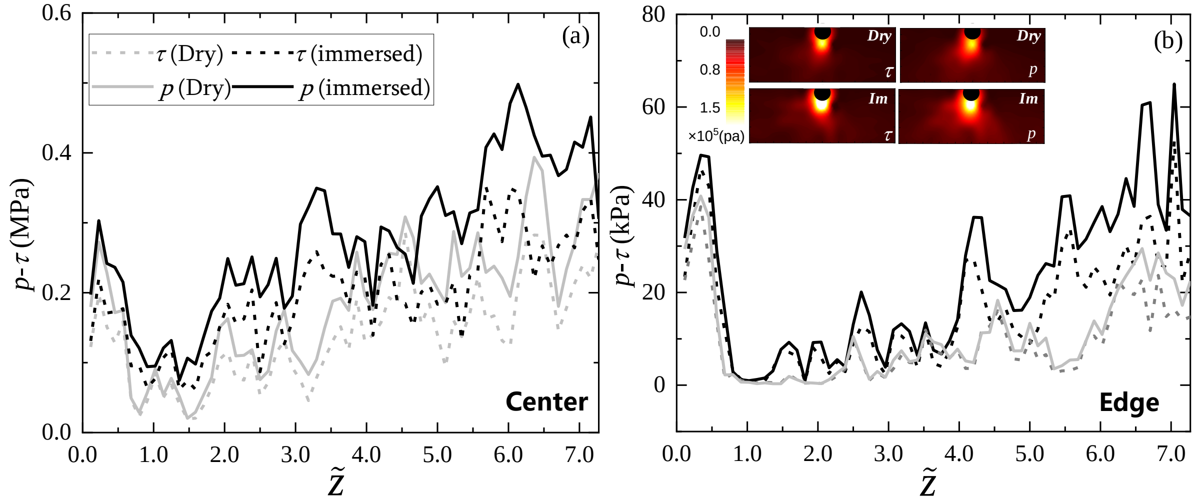

Fig 6 (a)-(b) the evolution of the shear stress (τ) and pressure (p) versus penetration depth $\tilde{Z}$ in different regions. The inset plot in (b) is the corresponding field distribution extracted from the position marked by the vertical red dashed line and the symbol is on the plot.

As one of the key granular properties, the granular temperature T has been considered to essentially affect the origin of the non-local behavior [46]. It could be defined as the mean square of the fluctuations of the particle velocity as $T = \langle (v - \langle v \rangle)^2 \rangle$ [47], where $\langle \dots \rangle$ computes the spatial averaged value. It can be further normalized as $T^* = T\rho/p$, where the p is the pressure. Fig 7 illustrates the variation of T^* and T in regions beneath and surrounding the intruder during the penetration process. The dimensionless temperature exhibits a rapid increasing trend in the transition stage which indicates the inertial granular flow. In addition, combined with the same evolution pattern of the inertial number, it could be derived that the T^* monitored is correlated to the inertial number as pointed out in the literature [47]. Regarding the spatial distribution feature, the granular material in the lateral position indicates a high inertial state with intense velocity fluctuations. As shown in the inset plot, after the initial contact stage, the non-dimensional granular temperature exhibits a nearly steady state, which is similar to the time evolution of the shear rate, and subsequently, this consistency states the strong correlation between the two variables. As a result, a stronger kinetic behavior has been observed in the lateral regions near the intruder both in the dry and immersed modelling scenarios. In the underneath region, the low temperature T^* is observed. The comparison indicates that the ambient fluid has a certain weakening impact on the dimensionless temperature, which originates from the constrained effect provided by the viscous interaction.

It needs to be noted that the granular temperature is related to the non-local behavior through the 'diffuse' process and induces 'creep' motion and destruction at some positions with relatively lower energy. The 'cooling' effect provided by the ambient fluid originates from the constraints of the particles' kinetic behavior, which has potentially changed the non-local behavior by decreasing the temperature gradient. However, this topic is beyond the scope of this work and could be investigated in future work.

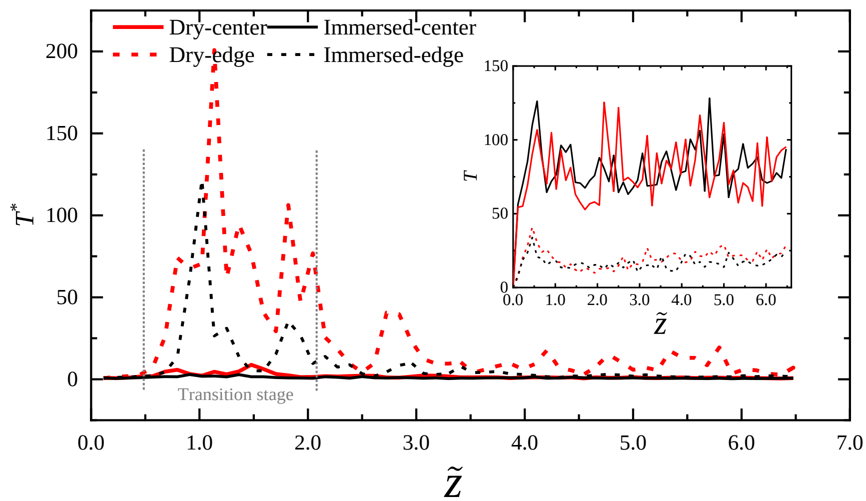

Fig 7. The dimensionless granular temperature (T^*) versus normalized depth($\tilde{z}$)in regions beneath and surrounding the intruder for the dry and immersed modelling scenarios. The inset plot shows the evolution of the granular temperature (T).

D. Rheological mechanism

The rheological characteristics of the granular media under the influence of the intruder are depicted in Fig 8, for the effective friction coefficient $\mu = \tau/p$, viscosity $\eta = \tau/\dot{\gamma}$, and the inertial number $I = |\dot{\gamma}|d/(P/\rho_s)^{0.5}$. The inertial number I provides comprehensive insights and aids in determining the granular flow regime, which is closely related to other granular properties mentioned in previous sections. In Fig 8(a), the inertial number I increases sharply at the intruder impact, and peaks quickly in the transition stage. The value of I in the region surrounding the intruder surpasses the inertial effect limit and eventually returns to the quasi-static state. During this process, the ambient fluid could significantly influence the flow regime of the granular bulk, where the momentum transfer between the fluid and particles slows down the granular flow dynamics through the viscous effect. As shown in the inset plot of Fig 8(a), the contour of the effective friction coefficient is demonstrated in the transition stage to reflect the correlation between μ and I in spatial distribution. It could be observed that the peak values emerge near the intruder, indicating the main agitated flowing region there. The comparative results of the contour between the immersed and dry cases are consistent with the evolution of inertial number. In the transition stage, the immersed granular materials present lower value of μ which is expected by the low inertial values illustrated by the main plot. In Fig 8(b), the time evolution of the viscosity is plotted, as contrary to the trend of inertial number I, the viscosity undergoes the descending and then recovering trend in the transition stage. The inset plot illustrates the spatial distribution of viscosity, in which the agitated region during the penetration process can be clearly identified. The observed peak value underneath the intruder of the immersed scenario indicates the low inertial region among the granular bed. Furthermore, the ambient fluid strengthened viscosity during the penetration process, resulting in a higher resistant force, especially with nearly the same shear rate as shown in Table 1.

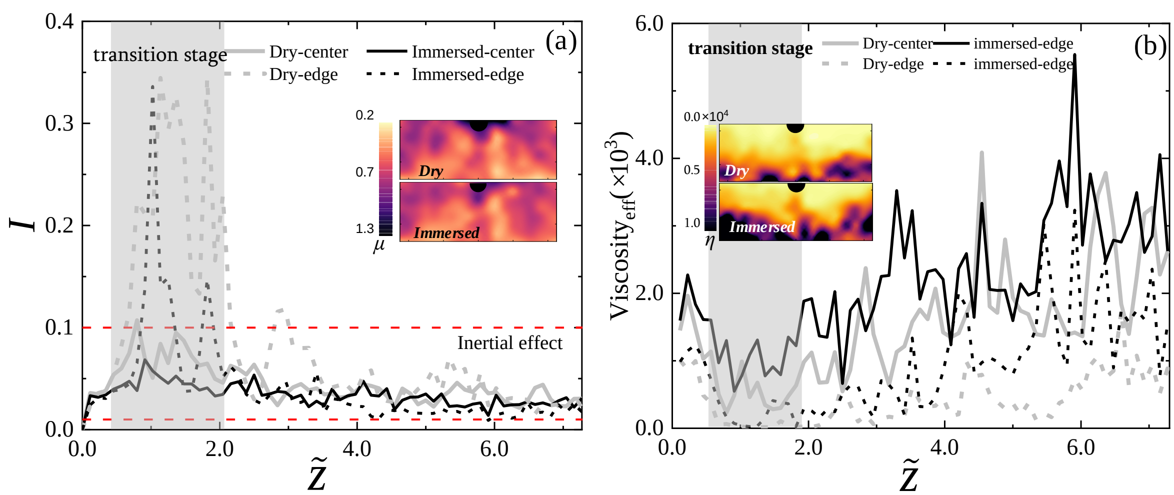

Fig 8. The evolution of the inertial number I (a) and the viscosity η (b) during the penetration process in the different regions(center, edge). The inset plots are the contour of the effective friction μ (in (a)) and η(in (b)) in the transition stage.

As shown in Fig 9(a), the parameters I and μ are non-linearly positively correlated, which aligns with the classical local rheology model $\mu(I) = \mu_s + (\mu_2 - \mu_s)/(I_0/I + 1)$ [48] qualitatively in both the immersed and dry cases. In Fig 9(b), the viscosity η and inertial number I follows a $\eta \sim I^{-2}$ scaling law. For the granular material, the transition of mechanical responses is always accompanied by the evolution of the granular structures, including the texture and the lifespan characteristic of the contact force. In line with the observed phenomenon, the corresponding structural evolution in the granular bulk during the penetration is revealed and interpreted by the coordination number C_n in Fig 9(c). A clear $C_n \sim I^{-1}$ scaling law between C_n and I is observed indicating a decreasing contact in the intensely flowing materials, which is consistent with the results reported in the literature [49]. Combining the evolution of I in Fig 8(a), it can be observed that after the initial contact stage with a relatively intact contact net, the region surrounding the intruder experiences intense fluidization, with some regions displaying extremely low coordination numbers. This indicates a complete suspension state wherein the collision becomes dominant. Finally, the C_n recovers in the depth-dependence stage, indicating the recurrence of the quasi-static regime. This analysis unveils the micro reflection of the inertial number I at the grain scale.

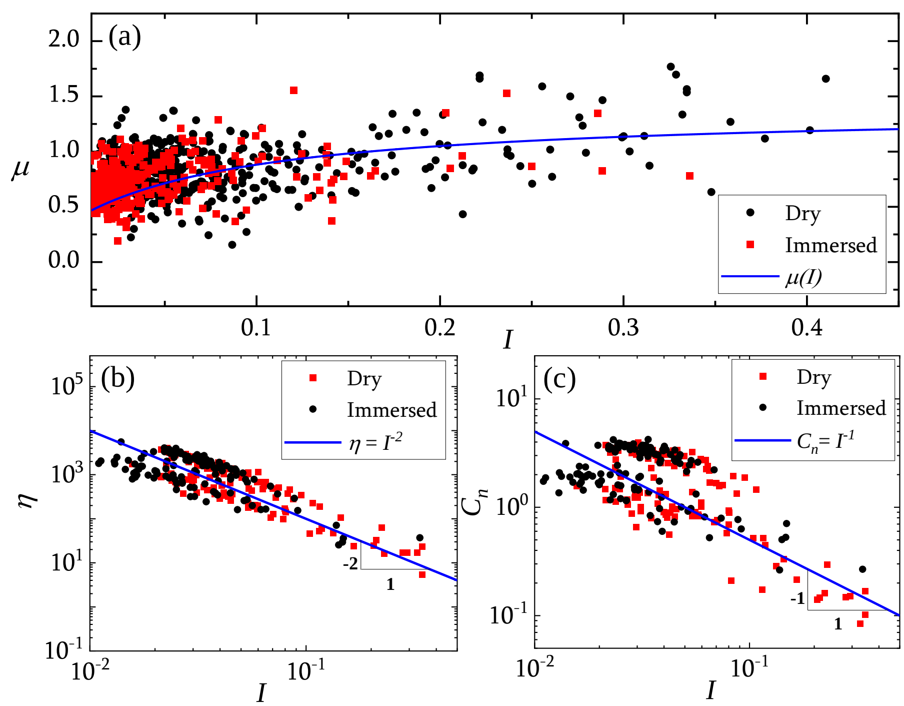

FIG 9.(a): The relationship between the I and μ, where the fitting curve (blue line) is the function $\mu(I) = \mu_s + (\mu_2 - \mu_s)/(I_0/I + 1)$. (b) - (c): the relationship between the viscosity η, coordination number C_n, and inertial number I

During the penetration, the ambient fluid restrains the flow dynamics of the granular material, specifically in the low inertial regime. However, it seems that the same rheological characteristic is shared between the dry and immersed cases, as illustrated in Fig 9(a). In essence, the combination of high η and low I led to the low dynamics of penetration stage for a $F \sim v_0$ relationship, while the combination of low η and high I facilitated the $F \sim v_0^2$ relationship for high penetration dynamics. This observation also reflects the decisive role of the Reynolds number Re_p in the drag force of Newtonian fluids for a gradually transition from laminar flow to turbulent flow as Re_p increases. These findings inspire a homology between I and Re_p in the granular intrusion process. It needs to be noted that the numerical simulations conducted in this research manifest the 'Fluid-inertial' regime according to the regime phase from the literature [50]. Therefore, the expected unified rheology of the $\mu - I$ correlation between the dry and immersed cases was observed, which has further validated our work. Meanwhile, the mechanism of penetration in the 'viscous' regime will be the next stage in the path approach to the complete unified theory/description.

Conclusions

The constant penetration in the granular bulk, both in the dry and immersed modelling scenarios, has been studied using a coupled numerical simulation model. Through the local rheology measurement, the dynamics of the drag force and its underlying mechanisms were explored. Various regimes were observed in the system, including the initial contact stage with $F_{peak} \sim v_0$ relationship, signifying the viscous behavior, followed by the transition stage characterized by fluidization and viscosity reduction. The depth-dependence regime showed a viscosity and inertial state recovery, and the proposed $F \sim \tilde{z}^2$ line aligned well with some existing published work. The evolution of local flow characteristics has been checked and the influence of the ambient fluid was investigated, revealing its constraining effect on granular flow dynamics, resulting in a lower inertial number I and granular temperature T^*. Nonlinear correlations in $\mu(I)$, $\eta(I)$, and $C_n(I)$ were evaluated and validated in both dry and immersed cases, indicating that the same rheology properties were shared by both scenarios. By disentangling velocity and depth-dependent contributions to the drag force, a general drag force evolution pattern unifying dry and immersed cases was proposed, which captures the common features ($F_{peak}=F(v)$, $z^* = F(v)$, and $F^*=F(v^2)$) and state the distinct mechanism from multi-scale perspective. Overall, The study provided new insights into the rheological mechanism in the penetration process for both dry and immersed granular material, and the unified characteristics of this phenomenon.

Acknowledgment

This research was supported, in whole or in part, by the Major Program of National Natural Science Foundation of China (Grant No. 51890911), the UK Engineering and Physical Sciences Research Council (EPSRC) New Investigator Award (Grant No. EP/V028723/1), Hainan Province Science and Technology Special Fund (Grant No. ZDYF2021SHFZ264), and the State Key Laboratory of Disaster Reduction in Civil Engineering (Grant No. SLDRCE19-A-06). The datasets generated during and/or analyzed during the current study are available from the corresponding author upon reasonable request

References

[1] H. Askari and K. Kamrin, Nature Materials **15**, 1274 (2016).
[2] M. Omidvar, J. D. Malioche, Z. Chen, M. Iskander, and S. Bless, Geotechnical Testing Journal **38**, 656 (2015).
[3] J. Aguilar and D. I. Goldman, Nature Physics **12**, 278 (2016).
[4] J. Aguilar *et al.*, Reports on Progress in Physics **79**, 110001 (2016).
[5] K. R. Housen and K. A. Holsapple, Icarus **163**, 102 (2003).
[6] P. Song and C. E. Choi, Journal of Geophysical Research: Earth Surface **126**, e2020JF005930 (2021).
[7] X.-s. Guo, T.-k. Nian, D. Wang, and Z.-d. Gu, Acta Geotechnica, 1 (2022).
[8] L. F. Jansa and G. Pe-Piper, Nature **327**, 612 (1987).
[9] S. Dunatunga and K. Kamrin, Journal of Fluid Mechanics **779**, 483 (2015).
[10] A. Seguin, Y. Bertho, P. Gondret, and J. Crassous, Phys Rev Lett **107**, 048001 (2011).
[11] A. Seguin, Y. Bertho, F. Martinez, J. Crassous, and P. Gondret, Phys Rev E **87**, 012201 (2013).
[12] W. T. Kang, Y. J. Feng, C. S. Liu, and R. Blumenfeld, Nat Commun **9** (2018).
[13] Y. Feng, R. Blumenfeld, and C. Liu, Soft Matter **15**, 3008 (2019).
[14] D. Van Der Meer, Annual Review of Fluid Mechanics **49**, 463 (2017).
[15] M. Tiwari, T. K. Mohan, and S. Sen, Phys Rev E **90**, 062202 (2014).
[16] H. Katsuragi and D. J. Durian, Nature Physics **3**, 420 (2007).
[17] D. I. Goldman and P. Umbanhowar, Phys Rev E **77**, 021308 (2008).
[18] P. Umbanhowar and D. I. Goldman, Phys Rev E **82**, 010301 (2010).
[19] Z. Peng, X. T. Xu, K. Q. Lu, and M. Y. Hou, Phys Rev E **80** (2009).
[20] C. S. Bester and R. P. Behringer, Phys Rev E **95**, 032906 (2017).
[21] L. T. Cisneros, V. Marzulli, C. Windows-Yule, and T. Pöschel, Phys Rev E **102**, 012903 (2020).
[22] X. Zhang, D. Zhang, Y. Wang, S. Ji, and H. Zhao, Granular Matter **25**, 1 (2023).
[23] R. Jewel, A. Panaitescu, and A. Kudrolli, Physical Review Fluids **3**, 084303 (2018).
[24] T. Hossain and P. Rognon, Physical Review Fluids **5**, 054306 (2020).
[25] S. Dunatunga and K. Kamrin, Journal of the Mechanics and Physics of Solids **100**, 45 (2017).
[26] T. A. Brzinski III, J. Schug, K. Mao, and D. J. Durian, Phys Rev E **91**, 022202 (2015).
[27] S. Agarwal, A. Karsai, D. I. Goldman, and K. Kamrin, Science Advances **7**, eabe0631 (2021).
[28] A. S. Baumgarten and K. Kamrin, Journal of Fluid Mechanics **861**, 721 (2019).
[29] L. K. Roth, Granular Matter **23**, 54 (2021).
[30] L. K. Roth, E. D. Han, and H. M. Jaeger, Phys Rev Lett **126** (2021).
[31] M. Jiang, Z. Shen, and J. Wang, Computers and Geotechnics **65**, 147 (2015).
[32] C. Kloss, C. Goniva, A. Hager, S. Amberger, and S. Pirker, Progress in Computational Fluid Dynamics, an International Journal **12**, 140 (2012).

[33] A. Seguin, Y. Bertho, and P. Gondret, Phys Rev E **78**, 010301 (2008).
[34] See Supplemental Material at [http://…] for detailed information about the numerical method, which includes Refs. [51-59].
[35] M. Jiang, J. Konrad, and S. Leroueil, Computers and geotechnics **30**, 579 (2003).
[36] N. Gravish, P. B. Umbanhowar, and D. I. Goldman, Phys Rev E **89**, 042202 (2014).
[37] F. Pacheco-Vazquez, G. A. Caballero-Robledo, J. M. Solano-Altamirano, E. Altshuler, A. J. Batista-Leyva, and J. C. Ruiz-Suarez, Phys Rev Lett **106** (2011).
[38] N. Gravish, P. B. Umbanhowar, and D. I. Goldman, Phys Rev Lett **105**, 128301 (2010).
[39] S. R. Waitukaitis and H. M. Jaeger, Nature **487**, 205 (2012).
[40] A. J. Liu and S. R. Nagel, Nature **396**, 21 (1998).
[41] D. D. Carvalho, N. C. Lima, and E. M. Franklin, Phys Rev E **105**, 034903 (2022).
[42] X. Ye and C. Zhang, Acta Mechanica Sinica **39**, 722198 (2023).
[43] M. B. Stone, R. Barry, D. P. Bernstein, M. D. Pelc, Y. K. Tsui, and P. Schiffer, Phys Rev E **70** (2004).
[44] A. Seguin, C. Coulais, F. Martinez, Y. Bertho, and P. Gondret, Phys Rev E **93**, 012904 (2016).
[45] M. Harrington, H. Xiao, and D. J. Durian, Granular Matter **22**, 1 (2020).
[46] J. Gaume, G. Chambon, and M. Naaim, Phys Rev Lett **125**, 188001 (2020).
[47] W. Han, H. Zhao, and D. Wang, Physics of Fluids **35** (2023).
[48] P. Jop, Y. Forterre, and O. Pouliquen, Nature **441**, 727 (2006).
[49] E. Azéma and F. Radjai, Phys Rev Lett **112**, 078001 (2014).
[50] K. F. Cui, G. G. Zhou, L. Jing, X. Chen, and D. Song, Physics of Fluids **32** (2020).
[51] P. A. Cundall and O. D. Strack, Geotechnique **29**, 47 (1979).
[52] R. Di Felice, International Journal of Multiphase Flow **20**, 153 (1994).
[53] J. Link, L. Cuypers, N. Deen, and J. Kuipers, Chemical Engineering Science **60**, 3425 (2005).
[54] J. Zhao and T. Shan, Powder Technology **239**, 248 (2013).
[55] L. Jing, C. Kwok, Y. F. Leung, and Y. Sobral, International Journal for Numerical and Analytical Methods in Geomechanics **40**, 62 (2016).
[56] C. K. Batchelor and G. K. Batchelor, *An introduction to fluid dynamics* (Cambridge university press, 1967).
[57] G. Q. Zhao and D. M. Wang, Powder Technology **374**, 1 (2020).
[58] A. Seguin, Granul Matter **22** (2020).
[59] A. Seguin, C. Coulais, F. Martinez, Y. Bertho, and P. Gondret, Phys Rev E **93** (2016).